JOBS
مجلة العلوم الأساسية
Journal of Basic Science
Print -ISSN 2306-5249
Online-ISSN 2791-3279
العدد السابع والاربعون
٢٠٢٦م /١٤٤٨هـ
العدد السابع والاربعون
(481) (445)

طريقة متكيّفة ذات بنية هار متناثرة باستخدام تحويل فورييه السريع للمعادلات التكاملية غير الخطية ثنائية البعد: الاستقرارية وضبط الخطأ والتحقق العددي

عبد الحكيم نايف مجيد
abdalhakeem2234@gmail.com

المستخلص:

تؤدي معادلات هامرشتاين وفريدهولم التكاملية غير الخطية ثنائية البعد إلى مؤثرات عددية مترابطة عالميًا، ولذلك يتطلب التقييم المباشر للنواة كلفة حسابية وخزنية تربيعية. يطوّر هذا البحث صياغة هار متناثرة متكيّفة مسرّعة بتحويل فورييه السريع (FFT–ASH) للنوى الدورية الثابتة انتقاليًا وللنوى غير الدورية القابلة للتضمين بالتمديد الصفري. تُحل المعادلة اللاخطية على مجموعة فعّالة من معاملات هار، في حين يُطبّق المؤثر اللاخطي وضرب المتجه اليعقوبي من دون تكوين مصفوفة كثيفة. تحت شرط الانكماش المعلن $q = |\lambda| \parallel G \parallel_1 L_\Phi < 1$، تُخصّص نتائج قياسية في النقطة الثابتة والاضطراب لإثبات حسن الوضع والاستقرارية وبناء شهادة خطأ قابلة للحساب من المتبقي، مع فصل حجم شبكة التضمين M عن عدد المعاملات الفعّالة N. تبلغ كلفة كل تقييم للمتبقي أو ضرب متجه يعقوبي $O(M\log M + N)$ والذاكرة العاملة $O(M + N)$. أظهرت الاختبارات سلوك تقارب من الرتبة الأولى؛ إذ انخفض خطأ L^2 من 2.139×10^{-2} إلى 2.673×10^{-3} عند زيادة M من ١,٠٢٤ إلى ٦٥,٥٣٦. احتفظ الاختبار الموضعي بنسبة ١٠.١٦% من المعاملات بخطأ نسبي ٠.٠٢١٥%، بينما احتفظ اختبار ضعيف التفرد بنسبة ٨٢.٨٦%، وهو ما يبيّن أن التناثر يعتمد على طبيعة المسألة. وتراوحت الزيادة المقاسة في سرعة مؤثر FFT مقارنة بالالتفاف الدائري المباشر بين ٤.١١ و 2.00×10^3 ضمن الشبكات المختبرة. وتشمل عملية التحقق أيضًا مثال هار ثنائي البعد منشورًا، واختبارات اضطراب، وتطبيقًا لحقل عصبي مع تنقيح شبكي. لذا تقتصر الاستنتاجات على نظام الانكماش المعلن، والنوى القابلة لتضمين FFT، ونطاق الشبكات المختبر.

JOBS مجلة العلوم الأساسية
Journal of Basic Science
Print -ISSN 2306-5249
Online-ISSN 2791-3279
العدد السابع والاربعون
٢٠٢٦م /١٤٤٨هـ

الكلمات المفتاحية: المعادلات التكاملية غير الخطية ثنائية البعد؛ موجات هار المتكيّفة؛ التقريب المتناثر ؛ تحويل فورييه السريع؛ تقدير الخطأ بالمتبقي.

An Adaptive Sparse Haar-Transform Method Using the Fast Fourier Transform for Two-Dimensional Nonlinear Integral Equations: Stability, Error Control, and Numerical Validation

Abdulhakeem Nayyef Majeed Majeed
abdalhakeem2234@gmail.com

Abstract

Two-dimensional nonlinear Hammerstein and Fredholm integral equations lead to globally coupled discrete operators, for which direct kernel evaluation requires quadratic arithmetic and storage. This study develops an adaptive sparse Haar–FFT (ASH-FFT) formulation for translation-invariant periodic kernels and for nonperiodic kernels that admit a zero-padded convolution embedding. The algorithm solves a nonlinear equation on an active Haar coefficient set, applying the nonlinear operator and Jacobian–vector products matrix-free on an embedding grid. Under the stated contraction condition $q = |\lambda| \parallel G \parallel_1 L_\Phi < 1$, established fixed-point and perturbation arguments are specialized to obtain well-posedness, stability, and a computable residual error certificate; the algorithm-specific analysis then separates the embedding-grid size M from the active coefficient count N. One residual or Jacobian–vector product costs $O(M\log M + N)$ operations and uses $O(M + N)$ working memory; the reduced expression $O(N\log N)$ applies only to graded/local implementations satisfying $M = O(N)$. In the reported tests, the piecewise-constant Haar approximation shows first-order behavior: the L^2 error decreases from 2.139×10^{-2} to 2.673×10^{-3} as M increases from 1,024 to 65,536. A localized nonlinear test retains 10.16% of the coefficients with a relative error of 0.0215%, whereas a weakly singular test retains 82.86%, showing that sparsity is problem dependent. Operator-level FFT speedups over direct circular convolution range from 4.11 to 2.00×10^3 on the tested grids. Validation also includes a published two-dimensional Haar benchmark, perturbation tests, and a grid-refined neural-

field example. The claims are therefore restricted to the stated contraction regime, FFT-embeddable kernels, and the tested grid range.

Keywords: two-dimensional nonlinear integral equations; adaptive Haar wavelets; sparse approximation; Fast Fourier Transform; residual error estimation.

Highlights

- The algorithm-specific contribution is an active-Haar nonlinear equation with matrix-free FFT residual and Jacobian–vector products.
- Established contraction and perturbation results are explicitly identified and cited; within the stated contraction regime, the residual provides a computable error certificate.
- The analysis separates the embedding-grid size M from the active coefficient count N; an $O(N\log N)$ claim is made only under an explicit graded/local implementation condition.
- Numerical evidence is reported under stated comparison protocols and includes convergence, localized and weakly singular cases, operator-level timing, a published benchmark, perturbations, and a neural-field application.

1 .Introduction

Two-dimensional nonlinear integral equations arise when the state at a point depends on a nonlocal response over a surface or spatial field. Representative settings include radiative transfer, viscoelastic response, population interaction, electromagnetic scattering, image formation, and continuum neural fields. Their numerical difficulty is not only the nonlinearity: after discretization, a general kernel couples every output degree of freedom to every input degree of freedom, producing a dense operator; for M spatial unknowns, one direct application is O(M^2) (Atkinson, 1997.)

Haar wavelets are attractive because they are orthonormal, compactly supported, inexpensive to transform, and naturally linked to piecewise-constant local resolution. Babolian and Shahsavaran (2009) and Aziz and Islam (2013) developed Haar formulations for nonlinear one-dimensional Fredholm and Volterra equations; Derili et al. (2012) extended Haar wavelets to linear two-dimensional Fredholm equations, and Yasmeen et al.

(2023) developed higher-order Haar variants. Recent adaptive Haar work in other numerical settings uses coefficient thresholding and multiresolution trees to refine only information-rich regions; Chowdhury et al. (2023), for example, reported a GPU-parallel adaptive Haar multiresolution implementation. Adaptive collocation for Fredholm equations has also been analyzed with mapped spectral bases (Abdennebi & Rahmoune, 2024). These studies establish adaptivity and localization as existing ideas, but they do not provide the active nonlinear Haar–FFT formulation considered here.

Recent numerical work on two-dimensional nonlinear integral equations includes Taylor collocation for linear and nonlinear Volterra equations (Laib et al., 2023), Boubaker operational matrices for nonlinear Fredholm/Volterra classes (Davaeifar & Rashidinia, 2023), Sinc successive approximation with convergence and stability analysis for nonlinear Fredholm equations (Kazemi, 2024), mapped Hermite functions for weakly singular Fredholm–Hammerstein equations (Wang & Zhang, 2025), and Lucas operational matrices for fractional partial Volterra equations (Gholami et al., 2026). These methods provide important accuracy and regularity benchmarks, but their global representations do not supply the same active Haar coefficient selection coupled to a matrix-free convolution operator.

Fast convolution supplies the required operator structure when the kernel is translation invariant. The discrete convolution theorem reduces one operator application from O(M^2) to O(MlogM), with the usual distinction between circular convolution and zero-padded linear convolution (Cooley & Tukey, 1965; Vico et al., 2016). Recent FFT-based Fredholm work also demonstrates fast Fourier/Hilbert-transform treatment of convolution equations (Germano et al., 2025). Fast wavelet algorithms and wavelet compression establish the multiresolution primitives (Beylkin et al., 1991; Cohen, 2003). The contribution here is not any one of those established ingredients, but their integration into a nonlinear active-Haar discretization with residual-driven refinement and a clearly scoped complexity analysis.

1.1 .Related-work comparison and terminology

For a transparent, nonexhaustive comparison, Table 1 uses two descriptive category labels. PBD denotes a global polynomial-basis discretization, such

JOBS
مجلة العلوم الأساسية
Journal of Basic Science
Print -ISSN 2306-5249
Online-ISSN 2791-3279
العدد السابع والاربعون
٢٠٢٦م /١٤٤٨هـ

as Boubaker, Taylor, or Lucas operational-matrix methods. EPB denotes an enriched, mapped, or spectral polynomial-basis discretization, such as Hermite interpolation, mapped Hermite functions, or mapped Legendre collocation. These labels organize the comparison and are not acronyms attributed to the cited authors.

Table 1. Position of the proposed method relative to representative Haar, adaptive, FFT, PBD, and EPB approaches.

Method / source	Equation class	Representation	Adaptive	Fast global operator	Analysis / limitation
Babolian & Shahsavaran (2009)	1D nonlinear Fredholm	Haar	No	No	Error analysis; no 2D fast operator
Derili et al. (2012)	2D linear Fredholm	2D Haar	No	No	Published benchmark; global kernel matrix
Davaeifar & Rashidinia (2023), PBD	2D nonlinear Fredholm/Volterra	2D Boubaker matrices	No	No	High-order global approximation; dense system
Karamollahi et al. (2021), EPB	Nonlinear Fredholm	Hermite interpolation	No	No	Convergence analysis; no adaptive 2D convolution
Khudhair et al. (2024)	Complex nonlinear integral equations	Periodic quasi-wavelets	No	No	Convergence and numerical comparison
Wang & Zhang (2025), EPB	2D weakly singular Hammerstein	Mapped Hermite basis	No	No	Exponential convergence near endpoint singularities
Gholami et al. (2026), PBD	2D fractional Volterra	Lucas matrices	No	No	High accuracy on fractional examples
Abdennebi & Rahmoune (2024), EPB	Second-kind Fredholm	Mapped Legendre collocation	Yes; mapped grid	No	Convergence/error analysis; not Haar or 2D FFT

JOBS مجلة العلوم الأساسية Journal of Basic Science
Print -ISSN 2306-5249
Online-ISSN 2791-3279
العدد السابع والاربعون
٢٠٢٦م /١٤٤٨هـ

Method / source	Equation class	Representation	Adaptive	Fast global operator	Analysis / limitation
Chowdhury et al. (2023)	2D shallow-water PDE	Adaptive Haar grid	Yes; threshold/tree	Not an integral operator	Adaptive Haar implementation; not an integral-equation method
Kazemi (2024)	2D nonlinear Fredholm	Sinc quadrature	No	No	Convergence/stability; global quadrature
Germano et al. (2025)	Convolution equations	Fourier/Hilbert transforms	No	Yes; FFT	Fast convolution; no active-Haar nonlinear adaptivity
Present ASH-FFT method	2D nonlinear Hammerstein	Active 2D Haar	Yes; residual marking	Yes; matrix-free FFT	Stability, certificate, convergence, cost, memory, benchmark

1.2 .Research gap

The literature review identifies a specific combination rather than claiming that adaptive, Haar, FFT, or nonlinear integral-equation methods are individually absent. To the authors' knowledge, none of the representative studies in Table 1 simultaneously provides: (i) an active two-dimensional Haar coefficient equation for a nonlinear convolution/Hammerstein operator; (ii) matrix-free FFT evaluation of both the nonlinear operator and Jacobian–vector products; (iii) full-residual Dörfler marking of inactive Haar coefficients; (iv) a computable residual-to-error certificate under an explicit contraction condition; (v) error and complexity accounting that keeps M and N separate; and (vi) validation against exact solutions, direct convolution, perturbations, and a published two-dimensional Haar benchmark. This statement is limited to the cited representative literature and to the precise combination above.

1.3 .Novelty and main contributions

The contribution is the following algorithm-specific coupling. Established mathematical tools are cited where used and are not claimed as new:

An active-coefficient reformulation of the nonlinear integral equation. Equations (7)–(8) change the discrete unknown, operator application, and refinement logic relative to a dense Haar matrix formulation.

A matrix-free FFT expression for the nonlinear residual and Jacobian–vector product, permitting projected Picard or Newton–Krylov iterations without assembling an M×M interaction matrix.

A full-residual coefficient indicator with standard Dörfler bulk marking, applied to inactive Haar modes and specified by a reproducible sorting and tie-breaking rule.

A provenance-aware analysis: standard contraction, perturbation, Haar approximation, Neumann series, Dörfler, and FFT results are cited; the algorithm-specific derivations are the active-map error transfer and the complexity accounting with separate variables M and N.

Quantitative validation under stated comparison criteria, including exact and discrete manufactured solutions, a localized case, a weakly singular case, perturbations, direct-versus-FFT operator timing, memory estimates, a published benchmark, and a neural-field application.

The method is not asserted to be universally superior. It is designed for translation-invariant or FFT-embeddable kernels and for solutions with compressible Haar coefficients. For globally analytic solutions, a high-order PBD or EPB method may converge faster; for endpoint-dominated singularities, mapped bases may be more effective. The targeted advantage of ASH-FFT is the combination of local coefficient control, a fast global operator, and residual-based certification within the stated contraction regime.

2 .Model problem and mathematical assumptions

2.1 .Nonlinear convolution-type integral equation

Let Ω=T^2={(x,y):0≤x<1, 0≤y<1} denote the two-dimensional unit torus. The periodic setting makes the FFT structure exact. A nonperiodic rectangular problem is handled by extending the data and kernel to a doubled grid and applying zero padding, which prevents circular wrap-around. The primary model is the nonlinear Hammerstein equation

u(x)=f(x)+λ∫_Ω^▒G (x-y) Φ(u(y)) dy,   x∈Ω.

JOBS مجلة العلوم الأساسية
Journal of Basic Science
Print -ISSN 2306-5249
Online-ISSN 2791-3279
العدد السابع والاربعون
٢٠٢٦م /١٤٤٨هـ

(١)

Define the convolution operator C by Cw=G*w and the fixed-point map T(v)=f+λCΦ(v). Here f is the prescribed forcing, λ is a scalar coupling parameter, G is the kernel, and Φ is the pointwise nonlinearity. The model reduces to a linear Fredholm equation when Φ(v)=v, includes saturating neural-field models when Φ(v)=tanh(βv), and admits polynomial nonlinearities on a bounded invariant interval.

2.2 .Assumptions

Table 2. Explicit assumptions used in the analysis and reported experiments

Label	Explicit assumption
A1	$G \in L^1(\Omega)$; for the normalized smooth tests, $\parallel G \parallel_1 = 1$. Weakly singular kernels are regularized and discretely normalized.
A2	Φ is Lipschitz on an invariant interval $I_B = [-B, B]$: $\lvert\Phi(a) - \Phi(b)\rvert \le L_\Phi \lvert a - b\rvert$. For $\Phi(u) = u^3$, $L_\Phi = 3B^2$ on I_B.
A3	$f \in L^2(\Omega) \cap L^\infty(\Omega)$, and T maps the closed ball $\mathcal{B}_B = \{v\colon \parallel v \parallel_\infty \le B\}$ into itself.
A4	The contraction number $q = \lvert\lambda\rvert \parallel G \parallel_1 L_\Phi$ satisfies $q < 1$.
A5	The embedding grid is $n \times n$ with $n = 2^J$ and $M = n^2$. Midpoint sampling is used; nonperiodic convolutions employ zero padding.
A6	For uniform convergence, $u \in H^s(\Omega)$, $0 < s \le 1$. For adaptive convergence, the best N-term Haar error is assumed to satisfy $\sigma_N(u)_2 \le C_{\mathrm{comp}} N^{-\alpha}$ for some $\alpha > 0$.
A7	The inexact nonlinear solve on each active set terminates with an active-space defect no larger than $\varepsilon_{\mathrm{nl}}$; refinement terminates when the full residual is at most $\varepsilon_{\mathrm{res}}$.

2.3. NORMS, RESIDUAL, AND SYMBOLS

$$\| v \|_2 = \left(\int_{\Omega} |v(\mathbf{x})|^2 \, d\mathbf{x} \right)^{1/2}, \qquad R(v) = v - f - \lambda G * \Phi(v). \tag{2}$$

Haar transform and adaptive sparse representation

3.1. ONE- AND TWO-DIMENSIONAL HAAR BASIS

The one-dimensional Haar scaling function is $\varphi(x) = 1$ on $0 \le x < 1$, and the mother wavelet is $\psi(x) = 1$ on $0 \le x < 1/2$, $\psi(x) = -1$ on $1/2 \le x < 1$, and zero elsewhere. At level j and translation k,

$$\psi_{j,k}(x) = 2^{j/2}\psi(2^j x - k), \qquad j \ge 0, \quad 0 \le k < 2^j. \tag{3}$$

The two-dimensional orthonormal system is formed by tensor products of scaling and wavelet functions. In discrete form, the fast Haar transform H_h applies pairwise averages and differences recursively in each coordinate and costs O(M) operations (Daubechies, 1992; Mallat, 2008). The implementation was checked on a random 64×64 field: the maximum inverse-transform error was 1.33×10^{-15}, and the norm discrepancy was 2.84×10^{-14}.

3.2. ACTIVE COEFFICIENT REPRESENTATION

Let A be an active index set and let $\mathbf{c} \in \mathbb{R}^N$ contain only the retained coefficients. The full coefficient array is $E_A\mathbf{c}$ and the reconstructed grid function is

$$u_A = H_h^{\mathsf{T}} E_A \mathbf{c}. \tag{4}$$

This definition separates the algebraic dimension N from the FFT embedding size M. A localized solution may have $N \ll M$, but the reference global convolution still requires FFT buffers of size M. Compact Haar support alone therefore does not make a globally supported integral operator $O(N)$; the saving is in the active nonlinear unknown and coefficient representation unless a separate local FFT realization is introduced.

3.3. RESIDUAL INDICATOR AND DÖRFLER MARKING

After an inexact active-space nonlinear solve, compute the full physical residual $R_h(u_A)$ and its Haar coefficients $\hat{r} = H_h R_h(u_A)$. For each inactive index μ∉A, define the indicator ημ=|rμ|². Order the inactive indicators from largest to smallest and choose the smallest set $\mathcal{M} \subset A^c$ whose cumulative energy satisfies Equation (5), with ties resolved by the fixed Haar-index order. This is the standard Dörfler bulk criterion (Dörfler, 1996), applied here to the full residual rather than only to the active-space defect

$$\sum_{\mu \in \mathcal{M}} |\hat{r}_\mu|^2 \geq \theta \sum_{\mu \notin A} |\hat{r}_\mu|^2, \qquad 0 < \theta < 1. \tag{5}$$

The active set is updated as $A \leftarrow A \cup \mathcal{M}$. Newly activated coefficients are initialized from the corresponding mapped residual entries only as a warm start; the nonlinear solve then recomputes the active solution. Optional tree closure can add parent coefficients, and optional coarsening can remove coefficients below $\varepsilon_{\mathrm{coarse}}$. For reproducibility, the reported experiments use direct bulk marking with neither tree closure nor coarsening. The active cap in Table 4 is a safeguard: a run is treated as certified only if the full residual tolerance is reached before the cap.

4. FFT-accelerated nonlinear formulation

4.1. DISCRETE CONVOLUTION BY FFT

For a translation-invariant sampled kernel, the discrete convolution is diagonal in Fourier space. With $\hat{G}_h = F_h G_h$ precomputed,

$$C_h w = F_h^{-1}(\hat{G}_h \odot F_h w). \tag{6}$$

A direct circular convolution evaluates M outputs, each involving M kernel terms, and therefore costs $O(M^2)$. Equation (6) uses the precomputed kernel spectrum, one forward transform of the current field, one pointwise multiplication, and one inverse transform, requiring $O(M\log M)$. For a nonperiodic n×n rectangle, the kernel and data are embedded on a zero-padded grid of at least (2n−1)×(2n−1), or a larger FFT-friendly size, so that circular wrap-around does not contaminate the physical domain (Vico et al., 2016). All timing results in Section 7.3 concern the periodic circular-convolution case.

JOBS مجلة العلوم الأساسية
Journal of Basic Science
Print -ISSN 2306-5249
Online-ISSN 2791-3279
العدد السابع والاربعون
٢٠٢٦م /١٤٤٨هـ

4.2. NEW ACTIVE-COEFFICIENT NONLINEAR EQUATION

Projecting the discrete fixed-point equation onto the active Haar subspace yields the central modified model

$$u_A = P_A[f_h + \lambda C_h \Phi(u_A)]. \tag{7}$$

In coefficient form, Equation (7) becomes

$$F_A(\mathbf{c}) = \mathbf{c} - R_A H_h\left[f_h + \lambda C_h \Phi\left(H_h^{\mathsf{T}} E_A \mathbf{c}\right)\right] = \mathbf{0}. \tag{8}$$

Equation (8) is the principal algorithm-specific discrete equation. Its implementation follows the same data path at every nonlinear evaluation: (1) inject the active vector c into an M-entry Haar coefficient array; (2) synthesize the M-grid field with the inverse Haar transform; (3) apply Φ pointwise; (4) convolve on the embedding grid by multiplying the Fourier transform by the precomputed kernel spectrum; (5) transform back, form the physical residual, and analyze it with the Haar transform; and (6) restrict active residual components to the nonlinear solve while using inactive components for marking. Thus, sparsity reduces the nonlinear unknown dimension and active coefficient storage, but the reference FFT remains an M-grid operation. Unlike a dense Haar Galerkin/collocation or PBD/EPB operational-matrix formulation, no M×M interaction matrix is formed.

4.3. MATRIX-FREE JACOBIAN-VECTOR PRODUCT

When Φ is differentiable, let $u_A = H_h^{\mathsf{T}} E_A \mathrm{c}$. Differentiating Equation (8) in a direction v gives

$$J_A(\mathrm{c})\mathrm{v} = \mathrm{v} - \lambda R_A H_h C_h\left[\Phi'(u_A) \odot \left(H_h^{\mathsf{T}} E_A \mathrm{v}\right)\right]. \tag{9}$$

Thus Newton–Krylov iterations require no explicit Jacobian. Each Jacobian–vector product follows the same inject–synthesize–pointwise multiply–FFT convolution–analyze–restrict pipeline. The numerical experiments use projected Picard iterations because all reported cases satisfy $q < 1$; Equation (9) is included for applications that require Newton–Krylov. No convergence claim is made here outside the contraction regime.

4.4. REPRODUCIBLE ALGORITHM

Algorithm 1. Adaptive sparse Haar-transform/FFT solver (ASH-FFT)

JOBS مجلة العلوم الأساسية
Journal of Basic Science
Print -ISSN 2306-5249
Online-ISSN 2791-3279
العدد السابع والاربعون
٢٠٢٦م/١٤٤٨هـ

1. Input: f_h, sampled or zero-padded kernel G_h, nonlinearity Φ, coupling parameter λ, initial active set A_0, Dörfler parameter θ, nonlinear tolerance $\varepsilon_{\mathrm{nl}}$, and residual tolerance $\varepsilon_{\mathrm{res}}$.
2. Precompute the kernel spectrum $\hat{G}_h = F_h G_h$. Initialize A with the 4×4 coarse Haar block and set $\mathrm{c} = R_A H_h f_h$.
3. Solve $F_A(\mathrm{c}) = 0$ inexactly by projected Picard iteration or matrix-free Newton–Krylov. For each evaluation, inject the active vector, synthesize the M-grid field, apply Φ pointwise, perform the FFT convolution, analyze the residual with the Haar transform, and restrict it to A.
4. Recover $u_A = H_h^{\top} E_A \mathrm{c}$; compute the full physical residual $R_h(u_A)$ and its Haar coefficients $\hat{r} = H_h R_h(u_A)$. Active entries drive the nonlinear correction, and inactive entries drive refinement.
5. If $\| R_h(u_A) \|_2 \leq \varepsilon_{\mathrm{res}}$, stop with the residual certificate. Otherwise, compute $\eta_\mu = |r_\mu|^2$ for $\mu \notin A$, sort the indicators in descending order, and choose the smallest inactive set M satisfying $\sum_{\mu \in \mathcal{M}} |\hat{r}_\mu|^2 \geq \theta \sum_{\mu \notin A} |\hat{r}_\mu|^2$; break ties by the fixed coefficient index.
6. Update $A \leftarrow A \cup \mathcal{M}$; initialize newly active coefficients from the mapped residual as a warm start; optionally remove coefficients below $\varepsilon_{\mathrm{coarse}}$; and return to Step 3. The reported experiments use no coarsening or tree closure.
7. Output: u_A, active coefficient count N, residual certificate $\| R_h(u_A) \|_2 / (1 - q)$, nonlinear/adaptive iteration counts, total case time, and operator timing reported separately.

JOBS مجلة العلوم الأساسية
Journal of Basic Science
Print -ISSN 2306-5249
Online-ISSN 2791-3279
العدد السابع والاربعون
٢٠٢٦م /١٤٤٨هـ

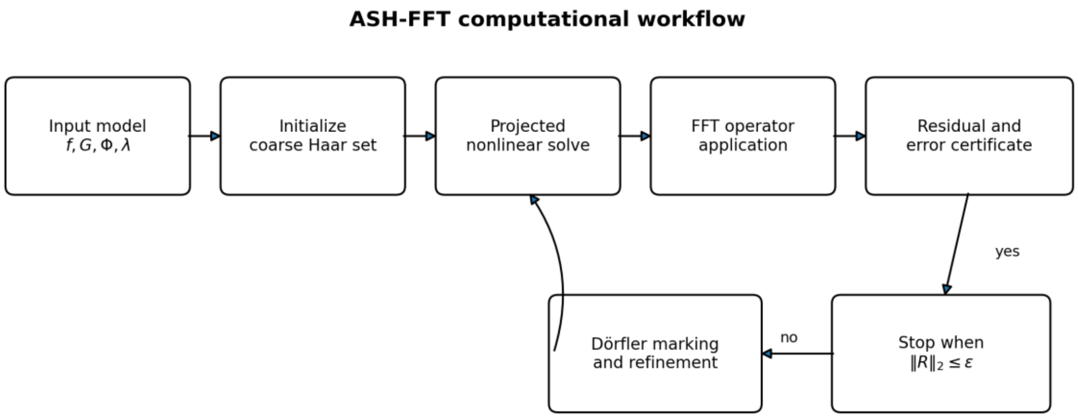

Figure 1. Schematic ASH-FFT workflow. The nonlinear solve uses active coefficients, whereas each convolution is evaluated on the embedding grid; the full residual supplies both the stopping certificate and the next marked set.

5. Mathematical analysis and provenance of results

Result-provenance statement.

Established ingredients (not claimed as new): Banach's fixed-point theorem and Picard convergence, Young's convolution inequality, orthonormal Haar approximation, Dörfler bulk marking, Neumann-series conditioning, and FFT operation counts (Atkinson, 1997; Folland, 1999; Kelley, 1995; Daubechies, 1992; Dörfler, 1996; Cooley & Tukey, 1965).

Algorithm-specific derivations in this paper: the active coefficient equations (7)–(9), their matrix-free residual/Jacobian–vector evaluation, the specialization of the residual certificate to the ASH-FFT map, the discrete error transfer in Equations (10)–(12) with separate M and N, and the per-evaluation complexity accounting in Theorem 4.

JOBS
مجلة العلوم الأساسية
Journal of Basic Science
Print -ISSN 2306-5249
Online-ISSN 2791-3279
العدد السابع والاربعون
٢٠٢٦م/١٤٤٨هـ

5.1.ESTABLISHED CONTRACTION RESULT SPECIALIZED TO THE MODEL

Theorem 1 (standard contraction result specialized to Equation (1)).
Under Assumptions A1–A4, $T(v) = f + \lambda G * \Phi(v)$ is a contraction on the invariant ball $\mathcal{B}_B$ with contraction number q. Consequently, Equation (1) has a unique solution $u \in \mathcal{B}_B$, and Picard iteration converges from every initial value in $\mathcal{B}_B$. This specialization uses the standard Banach fixed-point framework (Atkinson, 1997; Kelley, 1995).
Proof. For $v, w \in \mathcal{B}_B$, subtract the two fixed-point images. Young's convolution inequality gives $\| G * \big(\Phi(v) - \Phi(w)\big) \|_2 \le \| G \|_1 \| \Phi(v) - \Phi(w) \|_2$. Young's convolution inequality is used in its standard form (Folland, 1999).
The Lipschitz assumption then gives $\| T(v) - T(w) \|_2 \le |\lambda| \, \| G \|_1 \, L_\Phi \, \| v - w \|_2 = q \, \| v - w \|_2$. Because $q < 1$ and $T(\mathcal{B}_B) \subset \mathcal{B}_B$, the Banach fixed-point theorem yields existence, uniqueness, and geometric convergence.

$$\| u^{(m)} - u \|_2 \le \frac{q^m}{1 - q} \| u^{(1)} - u^{(0)} \|_2.$$

JOBS
مجلة العلوم الأساسية
Journal of Basic Science
Print -ISSN 2306-5249
Online-ISSN 2791-3279
العدد السابع والاربعون
٢٠٢٦م /١٤٤٨هـ

5.2. RESIDUAL CERTIFICATE AS A STANDARD CONTRACTION CONSEQUENCE

Theorem 2 (residual certificate; standard contraction consequence specialized here).

For every $v \in \mathcal{B}_B$, the residual $R(v) = v - f - \lambda G * \Phi(v)$ satisfies a two-sided estimate. This estimate is not claimed as a new abstract theorem; the contribution is its computable use for the ASH-FFT residual (Atkinson, 1997; Kelley, 1995).

Proof. Since $R(u) = 0$, write $R(v) = v - u - \lambda G * \big(\Phi(v) - \Phi(u)\big)$. The triangle inequality and the contraction estimate imply the upper bound.

For the lower bound, use the reverse triangle inequality: $\| R(v) \|_2 \geq \| v - u \|_2 - |\lambda| \, \| G \|_1 \, L_\Phi \, \| v - u \|_2 = (1 - q) \, \| v - u \|_2$. Rearranging yields the computable error certificate.

$$(1 - q) \| v - u \|_2 \leq \| R(v) \|_2 \leq (1 + q) \| v - u \|_2.$$

$$\| v - u \|_2 \leq \frac{\| R(v) \|_2}{1 - q}.$$

JOBS مجلة العلوم الأساسية
Journal of Basic Science
Print -ISSN 2306-5249
Online-ISSN 2791-3279
العدد السابع والاربعون
٢٠٢٦م /١٤٤٨هـ

5.3. STANDARD PERTURBATION ESTIMATE SPECIALIZED TO THE MODEL

Theorem 3 (data and kernel perturbations; standard contractive estimate specialized here).
Let u_1 and u_2 solve Equation (1) with data (f_1, G_1) and (f_2, G_2), while Φ and λ are fixed. If $q_\star = |\lambda| \max(\parallel G_1 \parallel_1, \parallel G_2 \parallel_1) L_\Phi < 1$ and $|\Phi(v)| \leq M_\Phi$ on the invariant ball, then the solution depends continuously on both f and G. The argument follows standard perturbation analysis for contractive integral operators (Atkinson, 1997).
Proof. Subtract the two equations, add and subtract $\lambda G_1 * \Phi(u_2)$, and apply Young's inequality. The term containing $u_1 - u_2$ is bounded by $q_\star \parallel u_1 - u_2 \parallel_2$.
Move that term to the left. The remaining terms are the forcing perturbation and the kernel perturbation acting on a bounded nonlinear response.

$$\parallel u_1 - u_2 \parallel_2 \leq \frac{\parallel f_1 - f_2 \parallel_2 + |\lambda| M_\Phi \parallel G_1 - G_2 \parallel_1}{1 - q_\star}.$$

5.4. ALGORITHM-SPECIFIC DISCRETE APPROXIMATION AND CONVERGENCE

Proposition 1 (ASH-FFT discrete error transfer).

Let T_h denote the sampled/FFT operator and P_A the orthogonal projection onto the active Haar space. The computed active solution satisfies $u_{A,h} = P_A T_h(u_{A,h})$ up to the nonlinear defect ε_{nl}. Add and subtract $P_A T(u)$, use the contraction estimate and nonexpansiveness of the projection, and obtain Equation (10).

$$\parallel u - u_{A,h} \parallel_2 \leq \parallel u - P_A u \parallel_2 + q \parallel u - u_{A,h} \parallel_2 + \delta_h + \varepsilon_{\text{nl}}. \quad (10)$$

Here δ_h bounds the consistency error $\parallel P_A[T(u_{A,h}) - T_h(u_{A,h})] \parallel_2$. Solving the resulting inequality yields Equation (11).

$$\parallel u - u_{A,h} \parallel_2 \leq \frac{\sigma_A(u)_2 + \delta_h + \varepsilon_{\text{nl}}}{1 - q}. \quad (11)$$

JOBS مجلة العلوم الأساسية Journal of Basic Science
Print -ISSN 2306-5249
Online-ISSN 2791-3279
العدد السابع والاربعون
٢٠٢٦م/١٤٤٨هـ

where $\sigma_A(u)_2 = \| u - P_A u \|_2$. For the complete uniform Haar space at level J, if $u \in H^s(\Omega)$ with $0 < s \leq 1$, standard piecewise-constant Haar approximation gives Equation (12) (Daubechies, 1992; Cohen, 2003).

$$\sigma_J(u)_2 \leq C 2^{-Js} |u|_{H^s(\Omega)} = C M^{-s/2} |u|_{H^s(\Omega)}. \quad (12)$$

For an adaptive active set with best N-term behavior $\sigma_N(u)_2 \leq C_{\text{comp}} N^{-\alpha}$, Equation (11) transfers the same algebraic rate up to consistency and nonlinear tolerances (Cohen, 2003; Schwab & Stevenson, 2011). This transfer bound is algorithm-specific, but the approximation classes and best-term estimates are established. No universal rate is claimed without the stated regularity or compressibility.

5.5. CONDITIONING FROM STANDARD TRANSFORM AND NEUMANN-SERIES BOUNDS

The discrete Haar transform is orthonormal and therefore has condition number one in the Euclidean norm (Daubechies, 1992; Mallat, 2008). With unitary FFT normalization, the Fourier transform is also norm preserving; the kernel multiplier contributes at most $\| G \|_1$ to the L^2 operator norm. Linearizing the fixed-point residual gives $J = I - \lambda C_h D_\Phi$. If $\| \lambda C_h D_\Phi \|_2 \leq q < 1$, the standard Neumann-series argument (Kelley, 1995) yields Equation (13).

$$\| J^{-1} \|_2 \leq (1-q)^{-1}, \qquad \| J \|_2 \leq 1 + q, \qquad \kappa_2(J) \leq \frac{1+q}{1-q}. \quad (13)$$

The conditioning bound deteriorates as q approaches one, predicting slower Picard convergence and stronger perturbation amplification. Section 7.5 verifies both effects numerically rather than reporting stability only as a theoretical statement.

JOBS
مجلة العلوم الأساسية
Journal of Basic Science
Print -ISSN 2306-5249
Online-ISSN 2791-3279
العدد السابع والاربعون
٢٠٢٦م/١٤٤٨هـ

5.6. PER-EVALUATION COMPUTATIONAL AND MEMORY COMPLEXITY

Theorem 4 (ASH-FFT per-evaluation complexity; algorithm-specific accounting).
Let $M = n^2$ be the FFT embedding-grid size and $N = |A|$ the active coefficient count. One nonlinear residual or Jacobian-vector product in Equations (8)–(9) requires $O(M\log M + N)$ arithmetic operations and $O(M + N)$ working memory. A direct dense convolution requires $O(M^2)$ operations and $O(M^2)$ matrix storage. This bound concerns one residual or Jacobian–vector evaluation, not the total nonlinear/adaptive solve, whose cost also depends on iteration and refinement counts.
Proof. Haar analysis and synthesis cost $O(M)$, nonlinear pointwise evaluation costs $O(M)$, and the forward/inverse FFT pair costs $O(M\log M)$. Restriction, injection, and active-vector operations cost $O(N)$. The FFT arrays and sampled field require $O(M)$ memory, while active metadata and coefficients require $O(N)$. The Haar and FFT component costs are standard (Cooley & Tukey, 1965; Mallat, 2008).
The reduced expression $O(N\log N)$ is valid only for a graded/local FFT realization that maintains $M = O(N)$. The experiments retain a full embedding grid, so their reported theory and timings use M and N separately.

6. Reproducible numerical methodology and comparison protocol

6.1. HARDWARE, SOFTWARE, AND TIMING PROTOCOL

All results were generated in double precision on an Intel Xeon Platinum 8573C environment with five logical processors visible and 5.9 GiB of memory. The implementation used Python 3.13.5, NumPy 2.3.5, and SciPy 1.17.0. Thread-count environment variables were fixed to one for timing consistency. FFT timings are medians of 20 repetitions for $n \leq 64$ and 10 repetitions for $n = 128$; direct circular-convolution timings are medians of five repetitions for $n \leq 64$ and two repetitions for $n = 128$. Setup and plotting time are excluded from operator timings.

JOBS مجلة العلوم الأساسية
Journal of Basic Science
Print -ISSN 2306-5249
Online-ISSN 2791-3279
العدد السابع والاربعون
٢٠٢٦م /١٤٤٨هـ

6.2. ERROR AND SPARSITY MEASURES

$$E_2 = \left[M^{-1}\sum_i |u_i - u_i^\star|^2\right]^{1/2}, \qquad E_\infty = \max_i |u_i - u_i^\star|. \tag{14}$$

$$E_\% = 100\frac{E_2}{\| u^\star \|_2}, \qquad \text{rate} = \log_2\left(\frac{E_2(n)}{E_2(2n)}\right), \qquad \text{sparsity}_\% = 100\frac{N}{M}. \tag{15}$$

For the smooth continuous test, the piecewise-constant Haar solution is compared with the exact solution at four subcell points in each coordinate, so the reported L^2 error measures the represented function, not only its cell-center samples. The relative error is defined by Equation (15), and all reported norms use the same midpoint quadrature and normalization. For discrete manufactured tests, the forcing is constructed with the same discrete convolution operator; this isolates active-set and nonlinear-solver error but does not test an independent quadrature discretization.

6.3. COMMON ADAPTIVE SETTINGS

Table 4. Adaptive settings and comparison controls.

Experiment	Parameters
Smooth exact solution	$\theta = 0.90$; $\varepsilon_{\text{nl}} = 10^{-9}$; $\varepsilon_{\text{res}} = 0.11/n$; active cap 85%
Localized nonlinear solution	$\theta = 0.90$; $\varepsilon_{\text{nl}} = 10^{-8}$; $\varepsilon_{\text{res}} = 2.0 \times 10^{-5}$; active cap 35%
Weakly singular kernel	$\theta = 0.95$; $\varepsilon_{\text{nl}} = 10^{-8}$; $\varepsilon_{\text{res}} = 3.0 \times 10^{-5}$; active cap 90%
Neural-field application	$\theta = 0.90$; $\varepsilon_{\text{nl}} = 10^{-8}$; $\varepsilon_{\text{res}} = 2.5 \times 10^{-5}$; active cap 45%
All adaptive cases	4×4 initial Haar block; no coarsening; maximum 24 adaptive cycles

JOBS مجلة العلوم الأساسية
Journal of Basic Science
Print -ISSN 2306-5249
Online-ISSN 2791-3279
العدد السابع والاربعون
٢٠٢٦م /١٤٤٨هـ

Experiment	Parameters
Direct-versus-FFT operator test	Identical sampled kernel, input field, precision, normalization, and grid; operator time only; medians over stated repeats; setup and plotting excluded
Published Haar benchmark	Same six evaluation points and absolute-error definition as Derili et al. (2012); n=32 matched; n=64 is an internal refinement check; no timing ranking
Adaptive manufactured tests	Certification requires the full residual tolerance; report residual, L2 error, relative error, N/M, adaptive cycles, and total case time when available
Cross-method interpretation	Quantitative comparison only for like-for-like tests; different kernels, norms, basis orders, hardware, or stopping rules are discussed qualitatively

6.4. COMPARISON PROTOCOL AND INTERPRETATION LIMITS

Each comparison addresses a different question. The direct-versus-FFT benchmark uses the same sampled kernel, input array, precision, normalization, and embedding grid; it reports operator time only, with setup and plotting excluded. The published Derili et al. (2012) comparison uses the same six evaluation points and absolute-error definition at n=32; the n=64 column is an internal refinement check, not a published competitor.

Adaptive cases are considered successful only when the full residual tolerance is met before the active cap. Tables report the residual, actual error when an exact or discrete manufactured solution is available, active fraction, adaptive cycles, and elapsed case time. Cross-paper methods with different kernels, norms, basis orders, hardware, or stopping rules are discussed qualitatively rather than ranked by wall-clock time or raw error.

Consequently, Section 7 supports observed convergence under the stated regularity, operator-level acceleration on the tested grids, and problem-dependent compression. It does not establish universal end-to-end superiority or asymptotic scalability beyond the measured range.

7. Numerical results and validation

7.1. SMOOTH MANUFACTURED SOLUTION AND CONVERGENCE

The first problem uses the periodic heat-kernel multiplier $\widehat{G}_{k,l} = \exp[-2\pi^2\sigma^2(k^2 + l^2)]$ with $\sigma = 0.06$, $\lambda = 0.30$, $\Phi(u) = u^3$, and exact solution $u^\star(x, y) = 0.55\sin(2\pi x)\sin(2\pi y)$. Because $\sin^3 z = (3\sin z - \sin 3z)/4$, the forcing is obtained analytically by applying the heat multiplier to the four Fourier modes in $(u^\star)^3$. On the invariant interval $|u| \leq 1$, $L_\Phi = 3$ and $q \leq 0.90$; the observed iterates remain in a smaller range, and all solves converge.

Table 5. Smooth manufactured solution under the Table 4 settings: convergence, residual, active size, percentage error, and total case time.

n	M	N	N /M (%)	Residual	L^2 error	Rate	Error (%)	Time (s)
32	1,024	806	78.71	1.593e-03	2.139e-02	—	7.778	0.011
64	4,096	2,450	59.81	1.609e-03	1.079e-02	0.987	3.924	0.022
128	16,384	10,125	61.80	5.065e-04	5.360e-03	1.010	1.949	0.088
256	65,536	41,492	63.31	1.604e-04	2.673e-03	1.004	0.972	0.385

The measured L^2 error decreases by approximately a factor of two whenever n doubles, and the rates remain between 0.987 and 1.010 over the four tested grids. This is consistent with the $M^{-1/2}$ rate predicted by Equation (12) for a piecewise-constant two-dimensional Haar approximation with $s = 1$. The percentage error falls from 7.778% to 0.972%. The active

JOBS
مجلة العلوم الأساسية
Journal of Basic Science
Print -ISSN 2306-5249
Online-ISSN 2791-3279
العدد السابع والاربعون
٢٠٢٦م /١٤٤٨هـ

fraction is not small because the sine product is globally supported; this intentionally nonlocalized test prevents the sparsity claim from relying only on a favorable localized example. The result is an empirical check over the stated resolutions, not evidence of a higher or universal rate.

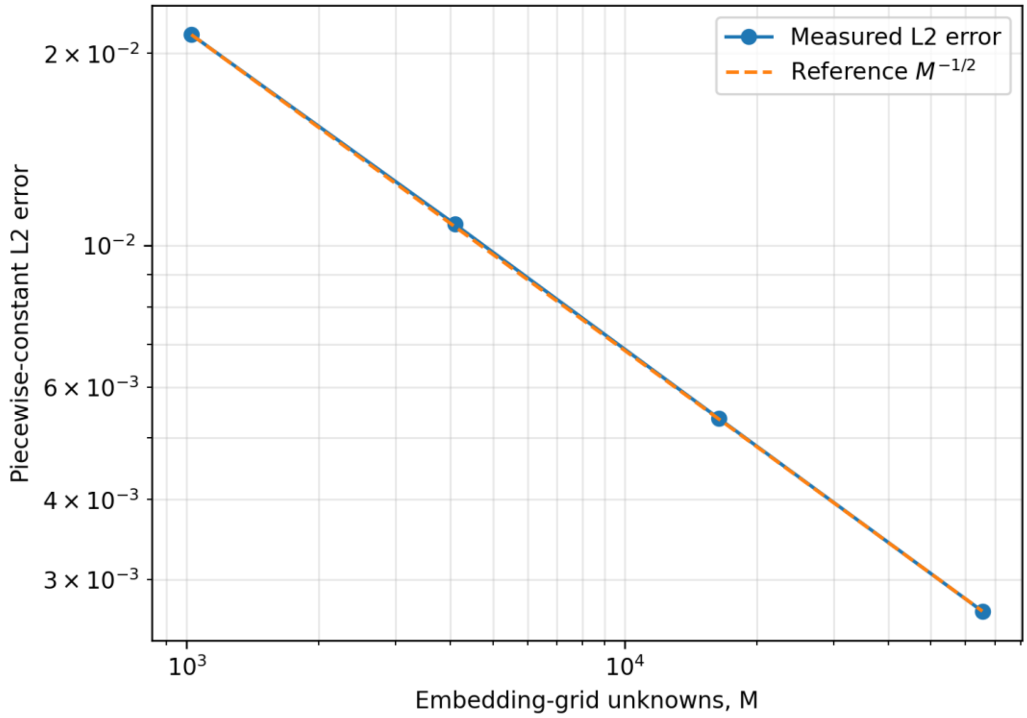

Figure 2. Log–log L2 error for the smooth manufactured solution. Over the four tested grids, the measured slope is consistent with the reference M−1/2 behavior.

7.2. LOCALIZED NONLINEAR SOLUTION AND ADAPTIVE COMPRESSION

Table 6. Adaptive results for localized and weakly singular nonlinear tests under the common stopping and active-cap conditions.

Case	n	q	N	N /M (%	Residual	L^2 error	L^∞ error	Error (%)	Cycles

JOBS
مجلة العلوم الأساسية
Journal of Basic Science
Print -ISSN 2306-5249
Online-ISSN 2791-3279
العدد السابع والاربعون
٢٠٢٦م /١٤٤٨هـ

Case	n	q	N	N/M (%	Residual	L^2 error	L^∞ error	Error (%)	Cycles
Localized tanh / Gaussian	256	0.567	6,659	10.16	1.617e-05	1.623e-05	1.797e-04	0.0215	8
Regularized weak singular/quadratic	256	local bound	54,304	82.86	2.070e-05	2.070e-05	8.568e-05	0.0073	7

For the localized case, $u^\star = 0.82\exp\left[-d_{\mathbb{T}}\left((x,y),(0.34,0.57)\right)^2/(2\times 0.052^2)\right]$, $\Phi(u) = \tanh(1.35u)$, $\lambda = 0.42$, and $\sigma = 0.035$. The forcing is constructed discretely. Only 6,659 of 65,536 coefficients (10.16%) are retained, while the L^2 error is 1.623×10^{-5} and the relative error is 0.02148%. The residual estimate in Section 5.2 gives the certificate 3.734×10^{-5} because $q = 0.567$, and the measured error lies below that bound.

The weakly singular test uses a normalized periodic kernel $G_\varepsilon(r) = C_\varepsilon(r^2+\varepsilon^2)^{-\alpha/2}$ with $\alpha = 0.65$ and $\varepsilon = 0.012$, $\Phi(u) = u^2$, and $\lambda = 0.22$. It attains a smaller relative error of 0.00731%, but requires 82.86% of the coefficients. This numerical result is important: weak singularity and the globally oscillatory component reduce Haar compressibility. The method remains accurate, yet its adaptive storage advantage is limited in this regime.

JOBS
مجلة العلوم الأساسية
Journal of Basic Science
Print -ISSN 2306-5249
Online-ISSN 2791-3279
العدد السابع والاربعون
٢٠٢٦م /١٤٤٨هـ

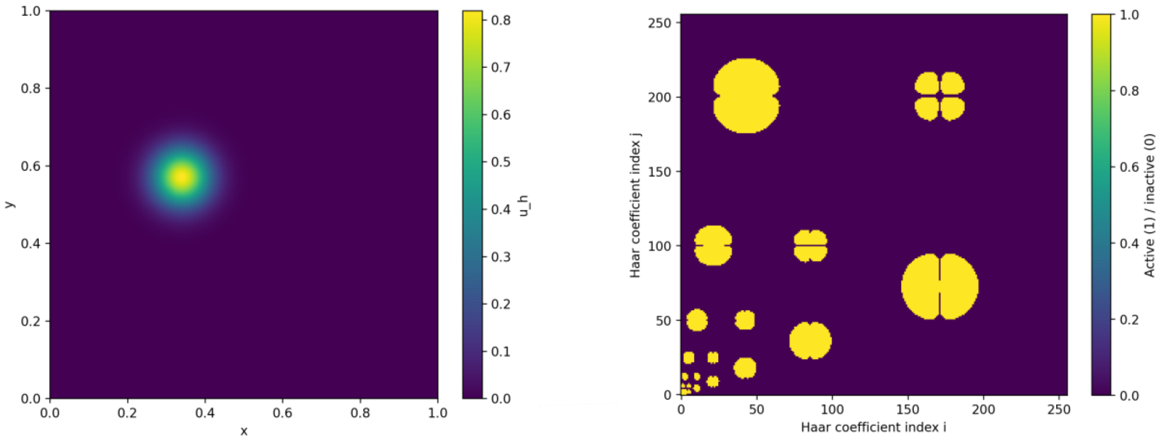

Figure 3. Localized nonlinear test: (left) computed solution; (right) active Haar coefficient mask. The marked set is concentrated around the localized features rather than spread uniformly over coefficient space.

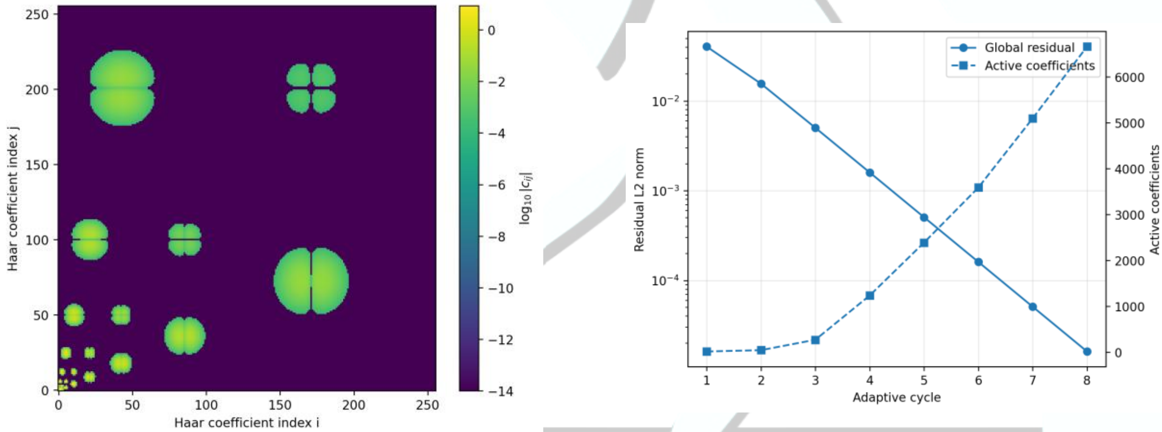

Figure 4. Localized nonlinear test: (left) magnitude of the Haar coefficients; (right) decrease of the full residual and growth of the active set over adaptive cycles.

JOBS
مجلة العلوم الأساسية
Journal of Basic Science
Print -ISSN 2306-5249
Online-ISSN 2791-3279
العدد السابع والاربعون
٢٠٢٦م /١٤٤٨هـ

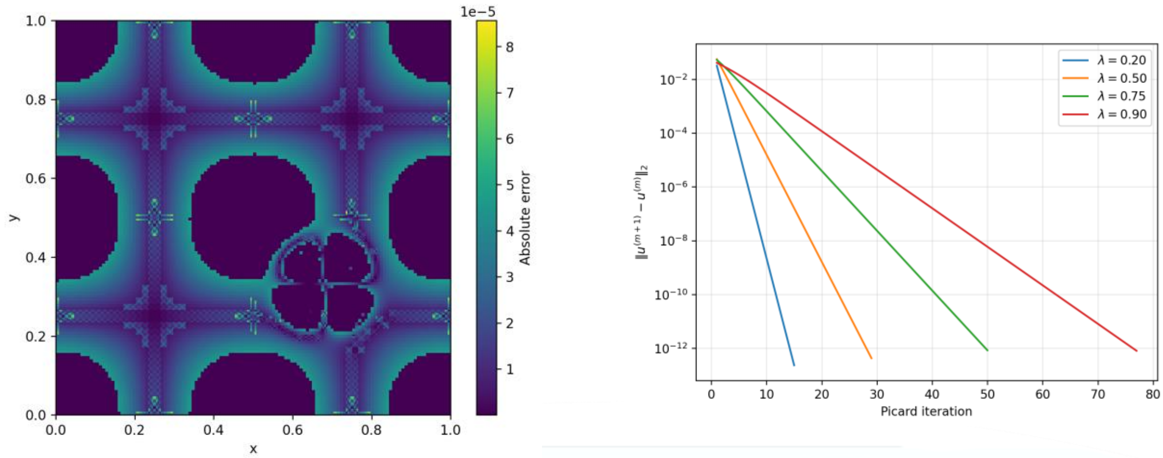

Figure 5. Weakly singular and stability tests: (left) absolute error for the weakly singular case; (right) Picard increment histories for four contraction parameters.

7.3. FFT COST AND MEMORY COMPARISON

Table 7. Operator-level convolution timing and analytical memory estimates (*eight real-equivalent M-sized work arrays).

n	M	FFT time (s)	Direct time (s)	Speedup	Dense MB	FFT MB*	Memory ratio
16	256	2.753e-05	1.130e-04	4.11	0.500	0.016	32
32	1,024	3.838e-05	1.751e-03	45.63	8.000	0.062	128
64	4,096	7.544e-05	3.318e-02	439.78	128.000	0.250	512
128	16,384	2.802e-04	5.609e-01	2002.16	2048.000	1.000	2048

JOBS
مجلة العلوم الأساسية
Journal of Basic Science
Print -ISSN 2306-5249
Online-ISSN 2791-3279
العدد السابع والاربعون
٢٠٢٦م /١٤٤٨هـ

At the tested size $M = 16{,}384$, the median FFT operator time is 2.802×10^{-4} s, whereas direct circular convolution requires 5.609×10^{-1} s, a measured speedup of approximately 2.00×10^{3} on the stated hardware. A dense $M \times M$ double-precision matrix would require 2,048 MB, while the eight-array FFT working estimate is 1 MB. This comparison concerns a single convolution application and an analytical storage model; it excludes Haar transforms, nonlinear iterations, marking, and adaptive-cycle overhead. It therefore supports operator acceleration, not an identical end-to-end speedup for the full solver.

JOBS
مجلة العلوم الأساسية
Journal of Basic Science
Print -ISSN 2306-5249
Online-ISSN 2791-3279
العدد السابع والاربعون
٢٠٢٦م /١٤٤٨هـ

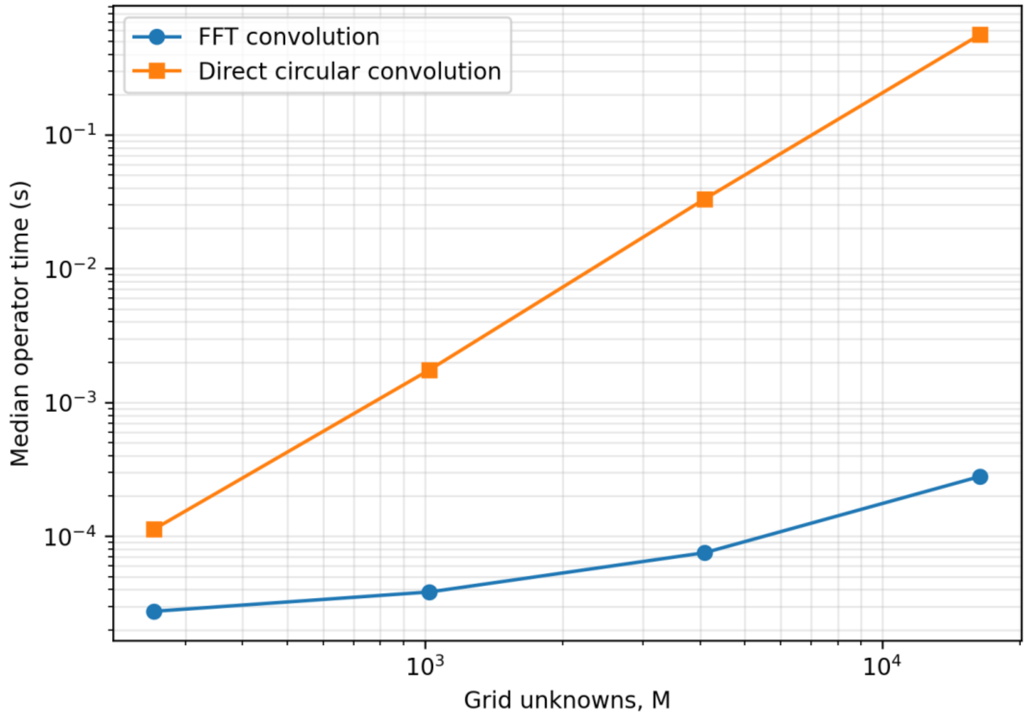

Figure 6. Operator-level median time for FFT and direct circular convolution on the measured grids. The widening separation is consistent with $O(M \log M)$ versus $O(M^2)$ operation counts; no extrapolation beyond the tested range is used.

7.4. VALIDATION AGAINST A PUBLISHED TWO-DIMENSIONAL HAAR BENCHMARK

Independent validation uses Example 1 of Derili et al. (2012): $u(x,y) = f(x,y) + \int_0^1 \int_0^1 (s\sin t + 1)\, u(s,t)\, ds\, dt$, with exact solution $u = x\cos y$ and $f = x\cos y - [\sin(1)(3 + \sin(1))]/6$. This kernel is nonconvolutional but rank one, so its integral is evaluated in $O(M)$. At n=32, the comparison uses the same piecewise-constant Haar interpretation, the same six evaluation points, and the same absolute-error criterion reported in the source. The n=64 column is included only to show internal refinement.

Table 8. Absolute-error comparison with the published Derili et al. (2012) 2D Haar benchmark.

l	x = y = 1/(2l)	Published k = 32	ASH representation n = 32	ASH representation n = 64
1	0.500000	8.600e-03	9.762e-03	4.932e-03
2	0.250000	1.200e-02	1.405e-02	7.056e-03
3	0.166667	8.900e-03	4.953e-03	2.506e-03
4	0.125000	2.000e-02	1.518e-02	7.610e-03
5	0.100000	6.000e-03	9.188e-03	1.531e-03
6	0.083333	4.300e-05	5.190e-03	2.568e-03
Mean	—	9.257e-03	9.720e-03	4.367e-03
Max.	—	2.000e-02	1.518e-02	7.610e-03

The $n = 32$ mean error is 9.720×10^{-3}, close to the published mean 9.257×10^{-3}, and its maximum error 1.518×10^{-2} is below the published maximum 2.000×10^{-2}. Refining to $n = 64$ reduces the mean and maximum to 4.367×10^{-3} and 7.610×10^{-3}. The agreement is not exact because the coefficient construction and point evaluation differ, but the same error scale and the systematic reduction under refinement provide an external reproducibility check. This comparison supports error-scale agreement only; implementation and hardware differences preclude a wall-clock or general accuracy ranking.

JOBS
مجلة العلوم الأساسية
Journal of Basic Science
Print -ISSN 2306-5249
Online-ISSN 2791-3279
العدد السابع والاربعون
٢٠٢٦م /١٤٤٨هـ

7.5. NUMERICAL STABILITY AND PERTURBATION AMPLIFICATION

Table 9. Perturbation behavior and Picard iteration counts as the contraction number approaches one.

λ	q	Picard iterations	Tail ratio	Measured amplification	Bound 1/(1−q)	Final L^2 error
0.20	0.20	15	0.160	1.236	1.250	4.392e-14
0.50	0.50	29	0.399	1.914	2.000	2.814e-13
0.75	0.75	50	0.599	3.541	4.000	1.243e-12
0.90	0.90	77	0.719	7.277	10.000	2.045e-12

The test uses $\Phi(u) = \tanh(u)$, a normalized heat kernel, and a low-frequency forcing perturbation of norm 10^{-7}. As λ increases from 0.20 to 0.90, Picard iterations increase from 15 to 77 and the measured perturbation amplification rises from 1.236 to 7.277. Every amplification remains below the theoretical bound $1/(1-q)$, and the observed tail ratios remain below q. The experiment therefore confirms the predicted loss of robustness as q approaches one within the stated contraction regime.

7.6. PRACTICAL APPLICATION: A STATIONARY TWO-DIMENSIONAL NEURAL FIELD

A practical test uses the stationary Amari-type neural-field equation $u = I + \lambda G * \tanh(\beta u)$, a standard nonlocal model for spatially distributed neural activity (Amari, 1977; Lima & Buckwar, 2015). The coupling is a difference of two normalized Gaussian kernels, $G = G_{0.035} - 0.28G_{0.11}$, representing short-range excitation and broader inhibition. Parameters are $\lambda = 0.36$ and $\beta = 1.25$, giving the conservative contraction estimate

JOBS مجلة العلوم الأساسية
Journal of Basic Science
Print -ISSN 2306-5249
Online-ISSN 2791-3279
العدد السابع والاربعون
٢٠٢٦م /١٤٤٨هـ

$q \le 0.576$. The external input I is the sum of two localized Gaussian stimuli centered at (0.34,0.49) and (0.66,0.54).

Table 10. Grid-refinement results for the stationary two-dimensional neural-field application.

n	M	N	N/M (%	Residual	Peak	Peak location	Grid difference	Time (s)
128	16,384	6,501	39.68	2.138e-05	0.658682	(0.3398, 0.4883)	8.258e-05	0.068
256	65,536	20,187	30.80	2.078e-05	0.658602	(0.3418, 0.4902)	2.692e-05	0.264
512	262,144	55,961	21.35	2.057e-05	0.658937	(0.3408, 0.4893)	—	1.360

Across the tested grids, the peak activity remains between 0.65860 and 0.65894 and its location remains near (0.341, 0.489). The L^2 difference between successive-grid solutions decreases from 8.258×10^{-5} to 2.692×10^{-5}. Meanwhile, the active percentage falls from 39.68% at $n = 128$ to 21.35% at $n = 512$, indicating that the computed pattern remains localized as the embedding grid is refined. At $n = 512$, the residual is 2.057×10^{-5}, and the run retains 55,961 of 262,144 Haar coefficients. These observations concern n=128–512 and are not extrapolated beyond that range.

JOBS
مجلة العلوم الأساسية
Journal of Basic Science
Print -ISSN 2306-5249
Online-ISSN 2791-3279
العدد السابع والاربعون
٢٠٢٦م /١٤٤٨هـ

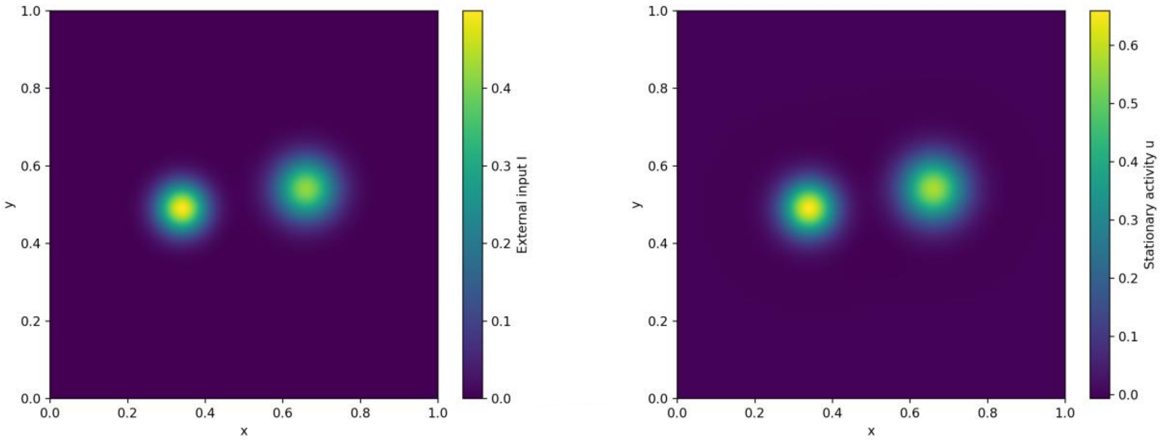

Figure 7. Neural-field application at n=512: (left) prescribed external input; (right) stationary activity after excitatory–inhibitory nonlocal coupling.

8. Discussion

8.1. WHAT IS MATHEMATICALLY NEW RELATIVE TO PBD AND EPB?

This contribution is not a new polynomial basis or a relabeling of standard Haar collocation. Equations (8)–(9) make the unknown an active Haar vector, evaluate the global nonlinear operator by FFT, and use unresolved residual energy to choose the next coefficient set. The contraction theorem, Dörfler marking principle, Haar approximation estimates, and FFT operation counts are established results and are now cited explicitly. The algorithm-specific contribution is their composition in the active nonlinear map, together with the discrete error transfer and separate M/N accounting.

For smooth analytic solutions, a spectral PBD/EPB method can achieve substantially higher order than the first-order Haar behavior in Table 5. For endpoint-dominated weak singularities, the exponential convergence reported for mapped Hermite functions is a stronger approximation property than piecewise-constant Haar. ASH-FFT is most appropriate when the kernel is FFT-embeddable, the solution contains localized or multiscale structure, active coefficient control is needed, and a residual certificate is valuable; even then, comparative performance depends on tolerances and implementation. This scoped statement replaces any universal “best method” claim.

8.2. INTERPRETATION OF ACCURACY, SPARSITY, AND SPEED

The experiments separate three effects. First, the smooth test checks the expected first-order Haar behavior. Second, the localized test demonstrates coefficient compression: 10.16% of the coefficients produce a 0.0215% relative error. Third, the convolution benchmark measures operator acceleration independently of adaptivity. The 2.00×10^3 speedup at the tested size $M = 16{,}384$ is attributable to FFT structure, not to Haar sparsity, and it is not presented as a full-solver speedup. This separation prevents distinct mechanisms from being conflated.

The weakly singular test is equally informative because it shows a negative result: 82.86% of the coefficients are required. The active representation is therefore not automatically sparse. A successful application requires either localized solution structure, coefficient decay, or a higher-order/mapped basis better matched to the singularity. This result defines the method’s practical boundary and explains when EPB alternatives should be considered.

8.3. NUMERICAL STABILITY AND VALIDATION STRENGTH

The stability experiment confirms two theoretical predictions numerically: iteration counts and perturbation amplification grow as q approaches one, while the observed amplification remains below $1/(1-q)$. Validation does not rely on manufactured solutions alone; it also includes a published two-dimensional Haar benchmark, a direct operator benchmark, a weakly singular kernel, grid refinement, and a neural-field model. Together these tests cover consistency, observed convergence, stability, external error-scale agreement, operator-level scaling over measured grids, and application behavior. They do not constitute a universal scalability study.

8.4. PRACTICAL LIMITATIONS AND EXTENSIONS

- Kernel structure: the FFT advantage requires translation invariance, periodicity, zero-padding embeddability, or an accurate

JOBS
مجلة العلوم الأساسية
Journal of Basic Science
Print -ISSN 2306-5249
Online-ISSN 2791-3279
العدد السابع والاربعون
٢٠٢٦م/١٤٤٨هـ

separable/convolutional approximation. General nonstationary kernels require a different fast representation, such as low-rank compression, hierarchical matrices, fast multipole methods, or localized block FFTs (Rokhlin, 1985; Vico et al., 2016).

• Approximation order: Haar functions are piecewise constant and therefore first order for H^1 solutions. Higher-order wavelets or multiwavelets naturally extend this to globally smooth solutions.

• Embedding memory: the active vector has N entries, but the reference implementation still stores M-sized FFT arrays. A true $O(N)$ working-memory result would require local or multilevel FFT blocks that maintain $M = O(N)$; that implementation is not used in the reported experiments.

• Nonlinearity: the proofs use $q < 1$. Problems outside the contraction regime require damped Newton–Krylov, continuation, or monotonicity arguments.

• Implementation: the numerical code prioritizes transparency and single-thread reproducibility. Parallel FFT libraries and GPU execution may reduce wall-clock time, but such acceleration is not measured here and would not change the mathematical discretization.

9. Conclusions

A scope-limited adaptive sparse Haar-transform/FFT framework has been formulated for two-dimensional nonlinear convolution-type integral equations. The revision explicitly separates established analytical ingredients from the algorithm-specific active-coefficient equations and their matrix-free composition. It also distinguishes the active coefficient count N from the embedding-grid size M; one residual or Jacobian–vector product has the stated $O(M\log M + N)$ cost and $O(M + N)$ working-memory bound. Under $q < 1$, the specialized analysis provides well-posedness, perturbation stability, residual-error equivalence, discrete error transfer, and conditioning estimates within the stated assumptions.

Within the tested ranges, the numerical evidence shows observed first-order Haar behavior, a localized case with 0.0215% relative error and 10.16% active coefficients, reduced compressibility for the weakly singular case, operator-level FFT speedup up to 2.00×10^3 at $M = 16{,}384$,

Print -ISSN 2306-5249
Online-ISSN 2791-3279
العدد السابع والاربعون
٢٠٢٦م /١٤٤٨هـ

perturbation amplification below the theoretical bound, comparable error scale on a published two-dimensional Haar benchmark, and stable neural-field peak/location under grid refinement. These results identify the method's promising regime—FFT-embeddable kernels and localized or multiscale solutions—but do not establish universal sparsity, end-to-end speedup, or scalability beyond the measured grids.

Declarations

Funding

No external funding was received for this study.

Conflict of interest

The author declares no conflict of interest.

Data and code availability

All numerical data in the tables and figures are generated from the equations, parameter values, tolerances, and hardware/software settings stated in the manuscript. The implementation and machine-readable result files are available from the author upon reasonable request.

Author contribution

Abdulhakeem Nayyef Majeed Majeed: conceptualization, methodology, mathematical analysis, software, validation, visualization, and writing.

References

1. Abdennebi, I., & Rahmoune, A. (2024). Adaptive spectral solution method for Fredholm integral equations of the second kind. Numerical Algorithms, 96, 975–998. https://doi.org/10.1007/s11075-023-01671-1

2. Amari, S. (1977). Dynamics of pattern formation in lateral-inhibition type neural fields. Biological Cybernetics, 27(2), 77–87. https://doi.org/10.1007/BF00337259

3. Atkinson, K. E. (1997). The Numerical Solution of Integral Equations of the Second Kind. Cambridge University Press.

4. Aziz, I., & Islam, S. (2013). New algorithms for the numerical solution of nonlinear Fredholm and Volterra integral equations using Haar wavelets. Journal of Computational and Applied Mathematics, 239, 333–345. https://doi.org/10.1016/j.cam.2012.08.031

5. Babolian, E., & Shahsavaran, A. (2009). Numerical solution of nonlinear Fredholm integral equations of the second kind using Haar wavelets. Journal of Computational and Applied Mathematics, 225(1), 87–95. https://doi.org/10.1016/j.cam.2008.07.003
6. Beylkin, G., Coifman, R., & Rokhlin, V. (1991). Fast wavelet transforms and numerical algorithms I. Communications on Pure and Applied Mathematics, 44(2), 141–183. https://doi.org/10.1002/cpa.3160440202
7. Chakir, Y., & Safouhi, H. (2024). Numerical solution of two-dimensional weakly singular Volterra integral equations of the first kind via bivariate rational approximants. Journal of Computational and Applied Mathematics, 436, 115378. https://doi.org/10.1016/j.cam.2023.115378
8. Chowdhury, A. A., Kesserwani, G., Rougé, C., & Richmond, P. (2023). GPU-parallelisation of Haar wavelet-based grid resolution adaptation for fast finite volume modelling: Application to shallow water flows. Journal of Hydroinformatics, 25(4), 1210–1234. https://doi.org/10.2166/hydro.2023.154
9. Cohen, A. (2003). Numerical Analysis of Wavelet Methods. Elsevier.
10. Cooley, J. W., & Tukey, J. W. (1965). An algorithm for the machine calculation of complex Fourier series. Mathematics of Computation, 19(90), 297–301. https://doi.org/10.1090/S0025-5718-1965-0178586-1
11. Daubechies, I. (1992). Ten Lectures on Wavelets. SIAM. https://doi.org/10.1137/1.9781611970104
12. Davaeifar, S., & Rashidinia, J. (2023). Operational matrix approach based on two-dimensional Boubaker polynomials for solving nonlinear two-dimensional integral equations. Journal of Computational and Applied Mathematics, 421, 114831. https://doi.org/10.1016/j.cam.2022.114831
13. Derili, H.-A., Sohrabi, S., & Arzhang, A. (2012). Two-dimensional wavelets for numerical solution of integral equations. Mathematical Sciences, 6, Article 5. https://doi.org/10.1186/2251-7456-6-5
14. Dörfler, W. (1996). A convergent adaptive algorithm for Poisson's equation. SIAM Journal on Numerical Analysis, 33(3), 1106–1124. https://doi.org/10.1137/0733054

15.Folland, G. B. (1999). Real Analysis: Modern Techniques and Their Applications (2nd ed.). Wiley.
16.Germano, G., Phelan, C. E., Marazzina, D., & Fusai, G. (2025). Solution of Wiener–Hopf and Fredholm integral equations by fast Hilbert and Fourier transforms. IMA Journal of Applied Mathematics, 90(4), 370–401. https://doi.org/10.1093/imamat/hxaf021
17.Gholami, S. S., Ebadian, A., Khajehnasiri, A. A., & Elgindy, K. T. (2026). A Lucas operational matrix method for solving nonlinear fractional two-dimensional partial Volterra integral equations. International Journal of Mathematics and Mathematical Sciences, 2026, 1183383. https://doi.org/10.1155/ijmm/1183383
18.Karamollahi, N., Heydari, M., & Barid Loghmani, G. (2021). Approximate solution of nonlinear Fredholm integral equations of the second kind using a class of Hermite interpolation polynomials. Mathematics and Computers in Simulation, 187, 414–432. https://doi.org/10.1016/j.matcom.2021.03.015
19.Kazemi, M. (2024). Sinc approximation for numerical solutions of two-dimensional nonlinear Fredholm integral equations. Mathematical Communications, 29(1), 83–103.
20.Kelley, C. T. (1995). Iterative Methods for Linear and Nonlinear Equations. SIAM. https://doi.org/10.1137/1.9781611970944
21.Khudhair, A. A., Sohrabi, S., & Ranjbar, H. (2024). Numerical solution of nonlinear complex integral equations using quasi-wavelets. AIMS Mathematics, 9(12), 34387–34405. https://doi.org/10.3934/math.20241638
22.Laib, H., Boulmerka, A., Bellour, A., & Birem, F. (2023). Numerical solution of two-dimensional linear and nonlinear Volterra integral equations using Taylor collocation method. Journal of Computational and Applied Mathematics, 417, 114537. https://doi.org/10.1016/j.cam.2022.114537
23.Lima, P. M., & Buckwar, E. (2015). Numerical solution of the neural field equation in the two-dimensional case. SIAM Journal on Scientific Computing, 37(6), B962–B979. https://doi.org/10.1137/15M1022562

24.Mallat, S. (2008). A Wavelet Tour of Signal Processing: The Sparse Way (3rd ed.). Academic Press. https://doi.org/10.1016/B978-0-12-374370-1.X0001-8
25.Rokhlin, V. (1985). Rapid solution of integral equations of classical potential theory. Journal of Computational Physics, 60(2), 187–207. https://doi.org/10.1016/0021-9991(85)90002-0
26.Schwab, C., & Stevenson, R. (2011). Adaptive wavelet algorithms for elliptic PDEs. Mathematics of Computation, 80(274), 1293–1323. https://doi.org/10.1090/S0025-5718-2011-02458-0
27.Vico, F., Greengard, L., & Ferrando, M. (2016). Fast convolution with free-space Green's functions. Journal of Computational Physics, 323, 191–203. https://doi.org/10.1016/j.jcp.2016.07.028
28.Wang, M., & Zhang, Z. (2025). Mapped Hermite functions and their applications to two-dimensional weakly singular Fredholm–Hammerstein integral equations. Journal of Computational and Applied Mathematics, 465, 116585. https://doi.org/10.1016/j.cam.2025.116585
29.Yasmeen, S., Siraj-ul-Islam, & Amin, R. (2023). Higher order Haar wavelet method for numerical solution of integral equations. Computational and Applied Mathematics, 42, Article 147. https://doi.org/10.1007/s40314-023-02283-0